Journal of Catalysis **210,** 67–83 (2002)
doi:10.1006/jcat.2002.3659

Bulk Structural Investigation of the Reduction of MoO_3 with Propene and the Oxidation of MoO_2 with Oxygen

T. Ressler,*,[1] J. Wienold,* R. E. Jentoft,* and T. Neisius†

*Fritz-Haber-Institut d. MPG, Department of Inorganic Chemistry, Faradayweg 4-6, D-14195 Berlin, Germany; and †European Synchrotron Radiation Facility, BP 220, F-38043 Grenoble Cedex, France

Received November 29, 2001; revised February 28, 2002; accepted April 23, 2002

Reduction of MoO_3 in propene and oxidation of MoO_2 in oxygen are investigated by *in situ* X-ray diffraction (XRD) and X-ray absorption spectroscopy (XAS). Temperature-programmed and isothermal experiments (573–773 K) are performed to elucidate the structural evolution of phases present during the reactions and, in addition, to reveal the solid-state kinetics of the processes involved. During the reduction of MoO_3 in propene and the oxidation of MoO_2, only crystalline MoO_3 and MoO_2 were detected by *in situ* XRD. The formation of a "$Mo_{18}O_{52}$"-type shear structure as intermediate during reduction of MoO_3 in propene and during oxidation of MoO_2 in oxygen was observed by *in situ* XAS. The solid-state kinetics of the reduction of MoO_3 in propene exhibits a change in the rate-limiting step as a function of both temperature and extent of reduction. The solid-state kinetics of the oxidation of MoO_2 is governed by three-dimensional diffusion. A schematic reaction mechanism for the reduction of MoO_3 in propene and reoxidation in oxygen is proposed that consists of (i) generation of oxygen vacancies at the (100) or (001) facets by reaction with propene, (ii) vacancy diffusion in the MoO_3 bulk, (iii) formation of $Mo_{18}O_{52}$-type shear structures in the lattice, and (iv) formation and growth of MoO_2 nuclei. With respect to a redox mechanism for the partial oxidation of propene on MoO_3, three stages are distinguished. (i) at temperatures below ~600 K the participation of oxygen from the MoO_3 bulk is negligible. (ii) At temperatures between ~600 and ~700 K oxygen vacancy diffusion in the bulk is sufficient to make a redox mechanism feasible, affording a partially reduced MoO_3 under reaction conditions. (iii) At temperatures above ~700 K sufficiently fast oxygen diffusion in the lattice combined with rapid formation and annihilation of crystallographic-shear planes permits the participation of a considerable amount of the lattice oxygen of MoO_3 in the partial oxidation of propene.

Key Words: **molybdenum oxide; MoO_3; MoO_2; *in situ*; time resolved; XAFS; XAS; EXAFS; XRD; X-ray; diffraction; propene; catalysis; solid-state kinetics; reduction; oxidation; redox mechanism; Mars–van Krevelen.**

INTRODUCTION

Molybdenum oxide-based catalysts are extensively employed for the partial oxidation of alkenes both in industrial applications and in academic research. Therefore, the properties of a large variety of molybdenum-containing systems have been studied in detail, in particular to elucidate relationships between the structure of these systems and their catalytic behavior. A comprehensive review on selective oxidation on metal oxide catalysts including molybdenum oxides and molybdenum-containing binary oxides was recently published by Grzybowska-Swierkosz (1) and refers to a number of other review articles on the same subject (2–4).

The increasing complexity of multiple-component systems (binary or higher mixed oxides containing molybdenum and other metals) makes studies on the correlation between catalyst structure and behavior difficult. Thus, many of the studies conducted in the past used pure molybdenum oxides as model systems for mixed oxide "real catalysts." One of the "model reactions" investigated in detail is the partial oxidation of propene to acrolein on molybdenum trioxide, MoO_3. With respect to a reaction mechanism, it appears to be agreed that the reaction starts with adsorption of propene on the surface of the catalyst, abstraction of hydrogen, and the formation of an allylic species (5, 6). Subsequently, oxygen from the bulk of the catalyst may be incorporated into the allylic species, affording the partial oxidation product acrolein or the total oxidation product carbon dioxide. This mechanism is referred to as the redox mechanism (or Mars–van Krevelen mechanism (7)) and consists of alternating oxidation and reduction of the metal oxide catalyst surface and/or bulk. Varying degrees of participation of bulk oxygen in partial oxidation reactions have been reported in the literature. For the three oxides V_2O_5 (674–823 K), MoO_3 (873–1023 K), and WO_3 (973–1073 K) it was found that practically all of the oxygen from the bulk could be exchanged with $^{18}O_2$ and, hence, could participate in oxidation reaction proceeding on the surface of the catalysts (8–10).

The reduction of MoO_3 is a crucial step in the redox mechanism of partial oxidation reactions on this material, and therefore, the reduction of MoO_3 with propene and hydrogen has been studied to a large extent. Formation of partially reduced molybdenum "suboxides" during reduction

[1] To whom correspondence should be addressed. Fax: (+49) 30 8413 4405. E-mail: Ressler@fhi-berlin.mpg.de.

0021-9517/02 $35.00

has been reported as a result of the redox mechanism and the difference in rates of catalyst reduction and reoxidation (1). For oxidation of 1-butene over bismuth molybdate catalysts in the temperature range 750–840 K, Batist *et al.* suggested a mechanism consisting of a surface reaction followed by oxygen vacancy diffusion in the solid (11). However, it seems that only in the near stoichiometric region (MoO_{3-x}, with x close to zero) is reduction of MoO_3 compensated for by oxygen vacancies in the bulk. With increasing density of oxygen vacancies in the bulk, Gai-Boyes has shown by transmission electron microscopy that crystallographic-shear (CS) planes are the compensating for defects in the MoO_3 structure (12). Furthermore, oxidation of propene on the MoO_3 layer structure was reported to be structure sensitive. However, interpretation of the results presented in the literature is controversial (5, 13–17).

In addition to reduction of the metal oxide catalyst, reoxidation of the catalyst bulk is the other crucial step in the redox mechanism. The oxidation step needs to follow the reduction of the metal oxide by the alkene in order to replenish the oxygen in the bulk of the metal oxide catalyst. However, compared to investigations of the reduction of molybdenum oxides, much less can be found regarding the oxidation of molybdenum oxides with oxygen. It is suggested that oxidation of molybdenum suboxides to MoO_3 is only complete above a certain temperature (~700 K) and that some intermediate phases may be formed during oxidation (18, 19).

Investigations of the correlation between structure and reactivity of heterogeneous catalysts need to be performed *in situ* (i.e., under reaction conditions at elevated temperature and in a reactant atmosphere) with simultaneous monitoring of the catalyst structure and the gas phase composition (20). Of the bulk techniques which can be employed to study a catalytically active material *in situ*, we used X-ray diffraction (XRD) and X-ray absorption spectroscopy (XAS). In addition to steady-state investigations, both techniques permit experiments with a suitable time resolution to monitor the structural evolution of bulk phases and from that to elucidate the solid-state kinetics of reactions of the catalyst bulk (21–24).

In this work the complementary techniques *in situ* XRD (long-range bulk structure) and XAS (short-range bulk structure) are employed to elucidate phase compositions, structural evolution, and solid-state reaction kinetics of the reduction of MoO_3 with propene and the oxidation of MoO_2 with oxygen not readily available from conventional thermoanalytical investigations. Both isothermal and temperature-programmed experiments under various reactant concentrations are presented. A comprehensive mechanism for the reduction and the reoxidation of MoO_3 is proposed and the consequences of this mechanism for the partial oxidation of propene on MoO_3 are discussed.

EXPERIMENTAL

MoO_3 Preparation and Characterization

Molybdenum trioxide (MoO_3) was prepared by thermal decomposition of ammonium heptamolybdate (AHM), $(NH_4)_6Mo_7O_{24} \cdot 4H_2O$ (Aldrich Co.), in flowing synthetic air (RT to 773 K at 2 K/min, held for 2 h at 773 K). Commercially available MoO_2 (Aldrich Co.) and MoO_3 (Aldrich Co.) were used as purchased. Phase purity of the compounds used was verified by XRD. MoO_3 employed in this study is identical to that used in Ref. (25) (BET surface area of ~5 m^2/g; average crystallite size of ~75 nm). Scanning electron micrographs of MoO_3 obtained from thermal decomposition of AHM in air at 773 K exhibit a particle size of about 200 nm and only minor anisotropy in the crystal planes exposed.

X-Ray Diffraction

Ex situ X-ray diffraction measurements for phase analysis were conducted using a STOE transmission diffractometer STADI-P (Ge primary monochromator, Cu $K\alpha$ radiation) equipped with a position-sensitive detector. Crystalline-phase identification based on XRD patterns was aided by the ICDD-PDF-2 database. Lattice constant refinement and quantitative phase analysis were performed using the software PowderCell v2.3 (26). The accuracy of the quantitative phase analysis was verified using a series of mechanical mixtures of MoO_2 and MoO_3.

In situ XRD experiments were carried out in Bragg Brentano scattering geometry on a STOE STADIP P diffractometer equipped with a secondary monochromator (Cu $K\alpha$ radiation) and a scintillation counter operated in a stepping mode. The *in situ* cell consisted of a Bühler HDK S1 high-temperature diffraction chamber. Details of the XRD setup can be found elsewhere (25). The gas-phase composition at the cell outlet was analyzed online with a Pfeiffer Prisma 200 quadropole mass spectrometer in multiple ion detection mode. *In situ* XRD measurements were conducted under atmospheric pressure in flowing reactants (~100 ml/min total flow). The effective heating rate used in temperature-programmed experiments depends on the measuring time per diffraction pattern and is given with the experimental data in the following (see Table 1).

In Situ X-Ray Absorption Spectroscopy

For *in situ* XAS experiments the molybdenum oxides were mixed with boron nitride (ratio 1 : 4) and 37 mg of the mixture was pressed with a force of 1 ton into a 5-mm-diameter self-supporting pellet. The absorption jump, $\Delta\mu x$, at the Mo K edge was ~2. *In situ* XAS experiments were performed in transmission in a flow reactor (27) at atmospheric pressure in flowing reactants (30 ml/min). Temperature-programmed experiments were conducted at

a constant heating rate of 5 K/min. The product composition in the gas outlet was continuously monitored using a mass spectrometer in multiple ion detection mode (QMS200 from Pfeiffer) with a time resolution of ~2 s per spectrum. Further details about the experimental XAS setup can be found in Ref. (25).

In situ transmission XAS experiments were performed at the Mo *K*-edge (19.999 keV (28)) at beamline X1 at the Hamburger Synchrotron Radiation Laboratory, HASYLAB, using a Si(311) double-crystal monochromator in the "Quick-EXAFS" mode (29) (measuring time, ~2 min/scan). The storage ring operated at 4.4 GeV with injection currents of 150 mA. Time-resolved *in situ* XAS experiments were carried out at the Mo *K*-edge utilizing an energy-dispersive spectrometer (European Synchrotron Radiation Facility, ESRF, ID24 (30)) equipped with a curved Si(111) polychromator in a transmission mode (31) (measuring time, ~3 s/scan). The storage ring operated at 6.0 GeV with injection currents of 90 mA in a 16-bunch mode.

XAFS Data Analysis

X-ray absorption fine structure (XAFS) analysis was performed using the software package WinXAS v2.1 (32) following recommended procedures from the literature (33). Background subtraction and normalization were done by fitting linear polynomials to the pre- and postedge regions of an absorption spectrum, respectively. The Mo *K*-edge absorption threshold was determined from the first root in the first derivative of the near-edge region (XANES). Principal component analysis (PCA) was used to identify Mo oxide phases present during the reduction of MoO_3 and oxidation of MoO_2. Given a set of molybdenum reference spectra (Fig. 1), PCA can identify those references that constitute probable components in the original set of experimental XANES spectra. Subsequently, after determination of the number and types of phases present, a least-squares fitting procedure can be applied to obtain the fraction of each reference phase under oxidation/reduction conditions. Hence, XANES analysis can afford information on low-concentration (~1 wt%) or amorphous phases not readily available with XRD. Details on PCA and the numerical procedures employed can be obtained from the literature (34, 35).

Cubic splines were used to obtain a smooth atomic background, $\mu_0(k)$, and to extract the X-ray absorption fine structure (EXAFS) $\chi(k)$. The radial distribution function FT($\chi(k)$) was calculated by Fourier transforming the k^3-weighted experimental $\chi(k)$ function, multiplied by a Bessel window, into the *R* space. EXAFS data analysis was performed using theoretical backscattering phases and amplitudes calculated with the ab initio multiple-scattering code FEFF7 (36). Single-scattering and multiple-scattering paths in the employed model structures were calculated up

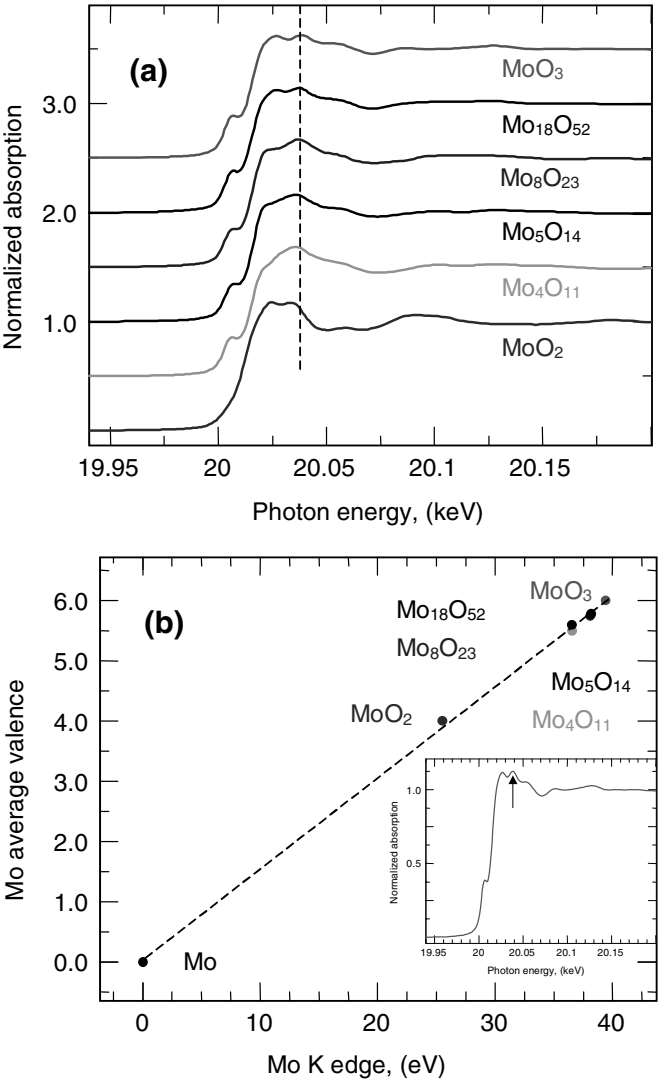

FIG. 1. (a) Mo *K* near-edge spectra of various molybdenum oxides used as references. The feature used to determine the *K*-edge position is indicated (inset). (b) Molybdenum average valence of the Mo oxide references in Fig. 1a as a function of the Mo *K*-edge position.

to 5.0 Å, with a lower limit of 2.0% in amplitude with respect to the strongest backscattering path.

EXAFS refinement was performed using the standard EXAFS formula (k range from 3.1 to 15.5 $Å^{-1}$; R range, 0.8–4.0 Å). Structural parameters that are determined by a least-squares EXAFS fit to the experimental spectra are (i) two E_0 shifts for oxygen and molybdenum backscatterers, (ii) two Debye temperatures for oxygen and molybdenum backscatterers, and (iii) distances of single-scattering paths, which were allowed to vary, and distances of multiple-scattering paths, which were correlated to the corresponding single-scattering paths. Coordination numbers (CN) were kept invariant in the refinement. EXAFS refinements reported here were conducted in *R* space to magnitude and

imaginary parts of a Fourier transformed k^3-weighted experimental $\chi(k)$. More details about the XAFS fitting procedure employed can be found in the literature (37, 23).

RESULTS

Molybdenum Oxide Reference Compounds

Mo *K* near-edge spectra of various molybdenum oxide references are shown in Fig. 1a. Details about the preparation of the reference compounds can be found elsewhere (38). The significant differences in the shapes of the spectra correspond to the different crystal structures of the molybdenum oxides. Hence, principal-component analysis of *in situ* time-resolved XAFS data can be readily employed to detect molybdenum oxides and suboxides during temperature-programmed or isothermal experiments. From the edge position of the spectra of the reference compounds a linear correlation with the average valence of molybdenum in these oxides was found, ranging from molybdenum metal to MoO_3. The magnitude of the shift in the Mo *K*-edge with the average Mo valence amounts to ~6.5 eV per increase in oxidation state by one.

Temperature-Programmed Reduction of MoO_3 with Propene

Temperature-programmed and isothermal reduction of MoO_3 with propene and oxidation of MoO_2 with oxygen was performed in different reactant concentrations and at different temperatures. A summary of the experiments conducted is given in Table 1. In the following, only a representative selection of the experiments shown in Table 1 are presented and discussed (highlighted in Table 1). The results of the studies not shown are consistent with the experiments and conclusions presented herein.

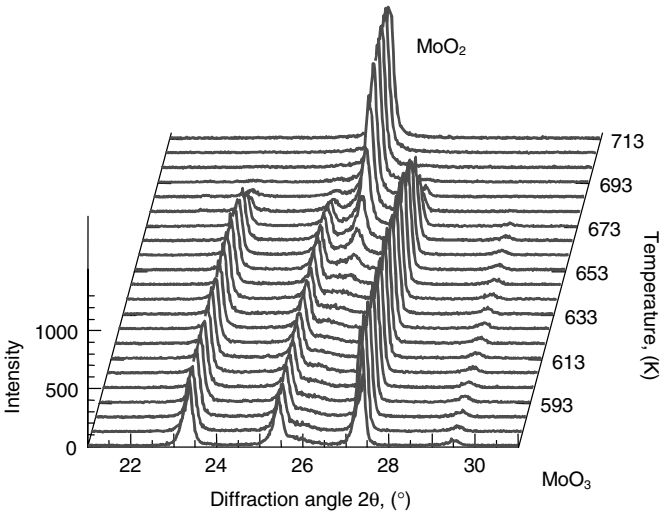

FIG. 2. *In situ* XRD during TPR of MoO_3 in 5 vol% propene in He from 573 to 713 K at a heating rate of 0.11 K/min (range in 2θ from 10 to 42°; temperature step size, 20 K; 1 h/scan, three scans at temperature). The two phases detected (MoO_2 and MoO_3) are indicated.

Figure 2 shows the evolution of X-ray diffraction patterns measured during temperature-programmed reduction (TPR) of MoO_3 in 5 vol% propene in He in the temperature range 573–713 K. While MoO_3 is completely reduced

TABLE 1

Reaction Conditions (vol% of Propene or Oxygen in He) and Measurement Conditions (*in Situ* Technique, Synchrotron Facility for XAS, Measuring Time per Scan) of *in Situ* Temperature-Programmed (Range and Heating Rate) and Isothermal (Temperature) XRD and XAFS Experiments during Reduction of MoO_3 with Propene and Oxidation of MoO_2 with Oxygen[a]

MoO_3	Temperature range and (effective) heating rate	Time/scan[b]	Isothermal reaction temperature in K							
			623	648	673	698	723	748	773	798
Reduction in propene										
5 vol% (XAS)	**300–773 K, 5 K/min**	**H, 2 min/scan**				**XX**	**XX**	**XX**	**XX**	
10 vol% (XAS)	**300–773 K, 5 K/min**	**H, 2 min/scan**		**XX**	**XX**	**XX**				
20 vol% (XAS)		E, 3 s/scan			XX	XX	XX	XX	XX	XX
40 vol% (XAS)		**E, 3 s/scan**		**XX**	**XX**	**XX**	**XX**	**XX**	**XX**	**XX**
5 vol% (XRD)	**573–713 K, 0.11 K/min**	**—**	**XX**	**XX**	**XX**					
Oxidation										
1 vol% (XAS)		**H, 2 min/scan**			**XX**	**XX**	**XX**	**XX**	**XX**	
5 vol% (XAS)	**300–773 K, 5 K/min**	**H, 2 min/scan**								
30 vol% (XAS)		E, 2 s/scan	XX	XX	XX	XX	XX	XX	XX	XX
50 vol% (XAS)		E, 2 s/scan	XX	XX	XX	XX	XX	XX	XX	XX
70 vol% (XAS)		E, 2 s/scan						XX	XX	XX
1 vol% (XRD)		—	**XX**	**XX**	**XX**	**XX**				
20 vol% (XRD)	**300–773 K, 0.2 K/min**	—								

[a] The experiments described in detail in this paper are bold in the table.
[b] E, ESRF; H, HASYLAB.

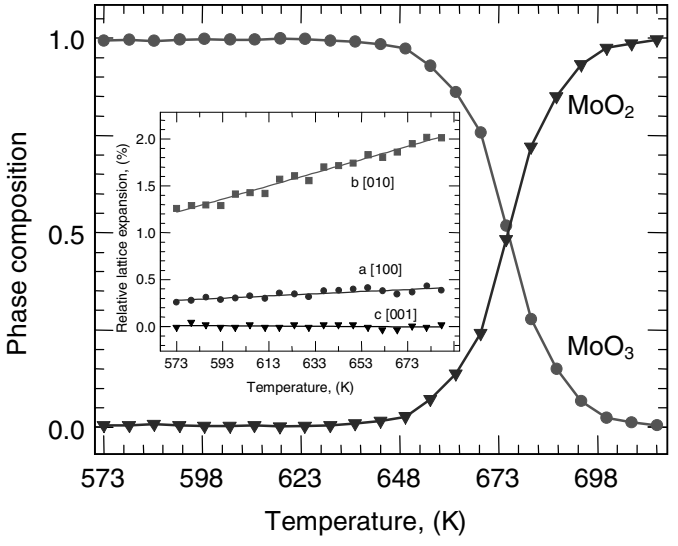

FIG. 3. Evolution of phase composition (MoO_2 and MoO_3) during TPR of MoO_3 in 5 vol% propene from 573 to 713 K (Fig. 2). The inset shows the evolution of the lattice constants of α-MoO_3 during TPR.

to MoO_2 only these two phases were detected by XRD. The corresponding change in phase composition (MoO_2 and MoO_3) during TPR of MoO_3 in 5 vol% propene is depicted in Fig. 3. The inset to Fig. 3 shows the evolution of the lattice constants of MoO_3 during TPR.

Evolution of Mo K-edge XANES spectra during TPR of MoO_3 in 10 vol% propene from 300 to 773 K at a heating rate of 5 K/min is presented in Fig. 4. A rapid transition between the near-edge spectra of MoO_3 and that of MoO_2 can be seen at ~673 K. The corresponding evolution of the

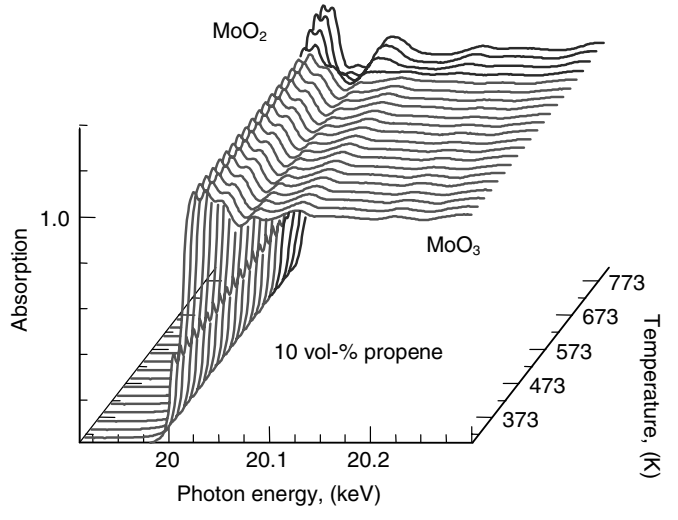

FIG. 4. *In situ* XAFS during TPR of MoO_3 in 10 vol% propene from 300 to 773 K at a heating rate of 5 K/min. The two most prominent phases (i.e., MoO_3 and MoO_2) are indicated.

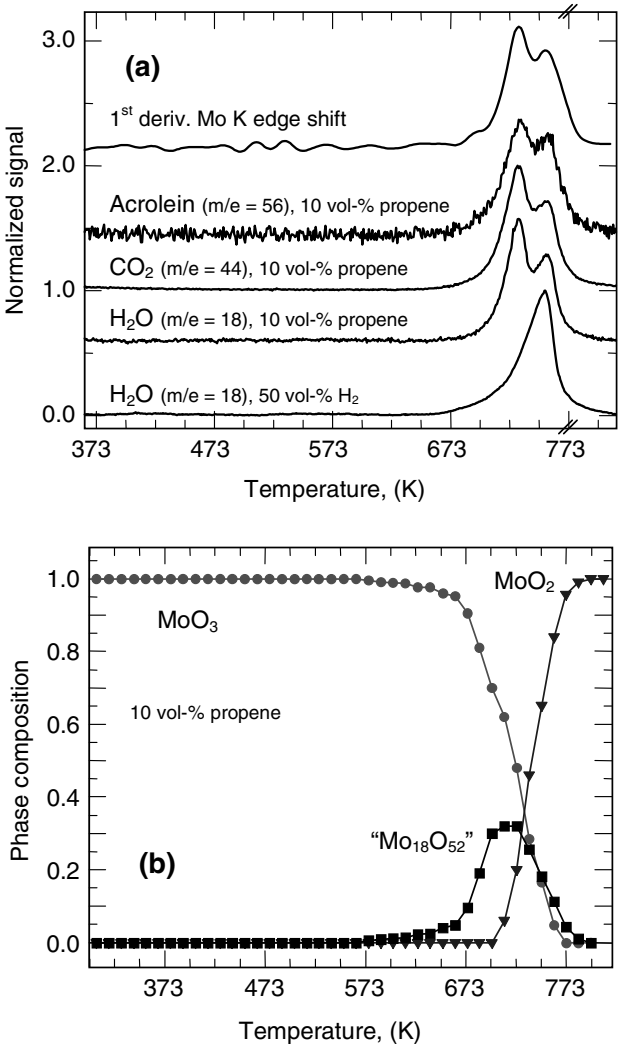

FIG. 5. (a) Evolution of Mo K-edge shift and of the concentration of acrolein ($m/e = 56$), CO_2 ($m/e = 44$), and H_2O ($m/e = 18$) in the gas phase during TPR of MoO_3 in 10 vol% propene from 300 to 773 K (Fig. 4). For comparison, the bottom trace shows the evolution of water ($m/e = 18$) during TPR of MoO_3 in 50 vol% H_2 (25). (b) Evolution of phase composition (MoO_3, MoO_2, and $Mo_{18}O_{52}$) during TPR of MoO_3 in 10 vol% propene (Fig. 4).

Mo K-edge shift and of the gas-phase composition (MS ion currents of H_2O, CO_2, and acrolein) is shown in Fig. 5a. For comparison, the evolution of water during the reduction of MoO_3 in 50 vol% hydrogen is also shown (experimental data from (23)). No formation of acrylic acid was detected under the experimental conditions employed. A principal-component analysis of the XANES spectra shown in Fig. 4 revealed the presence of at least three different phases during the reduction. Target transformation of the references listed in Fig. 1 showed MoO_3, MoO_2, and $Mo_{18}O_{52}$ to be suitable reference compounds for the three phases detected. A linear combination fit of the three reference spectra to the experimental XANES spectra resulted in the

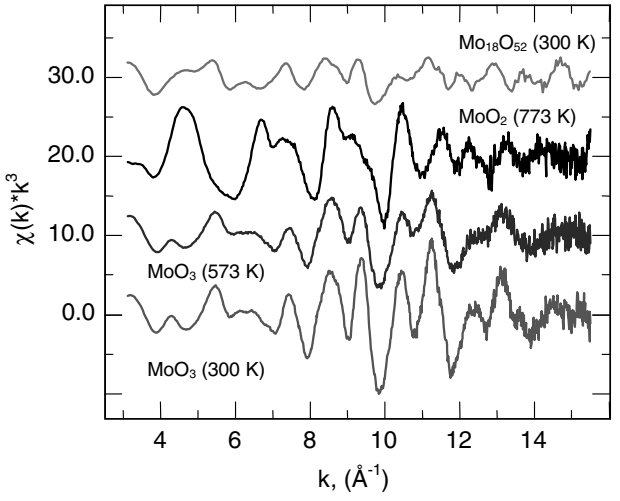

FIG. 6. XAFS $\chi(k)$ of MoO_3 at 300 K, MoO_3 at 573 K, MoO_2 at 773 K, and $Mo_{18}O_{52}$ at 300 K. XAFS spectra of MoO_2 and MoO_3 were measured in ~2 min in the energy range 19.9–21.0 keV.

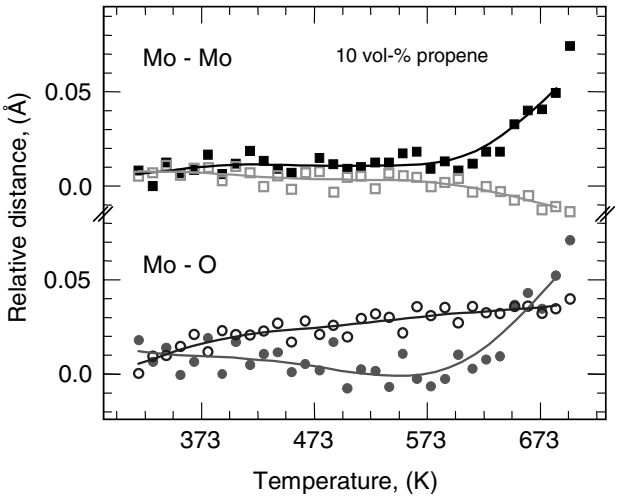

FIG. 8. Evolution of relative Mo–Mo and Mo–O distances in the MoO_3 structure during TPR of MoO_3 in 10 vol% propene from 300 to 773 K (Fig. 4). Distances shown are relative to the crystallographic distances in MoO_3 (Table 2). (Solid circles) Mo–O at 1.67 Å; (open circles) Mo–O at 1.74 Å; (solid squares) Mo–Mo at 3.44 Å; (open squares) Mo–Mo at 3.70 Å.

evolution of the three phases with temperature during reduction of MoO_3 in propene (Fig. 5b).

Experimental EXAFS $\chi(k)$ of molybdenum oxides at different temperatures (i.e., MoO_3 at 300 and 573 K, MoO_2 at 773 K, and $Mo_{18}O_{52}$ at 300 K) are depicted in Fig. 6. The spectra of MoO_2 and MoO_3 were obtained from *in situ* XAS experiments with a measuring time of about 2 min/scan. The data quality even at temperatures as high as 773 K is sufficient to permit a detailed EXAFS analysis up to $k = 15$ Å^{-1}. Figure 7 shows the evolution of Fourier transformed Mo K-edge $\chi(k)$ obtained from XAFS spectra measured during TPR of MoO_3 in 10 vol% propene (Fig. 4). At ~673 K a rapid transition between the FT($\chi(k)$) of MoO_3 and that of MoO_2 can be seen, preceded by a continuous decrease in amplitude of both the first and the second shell, mostly because of the increasing reaction temperature.

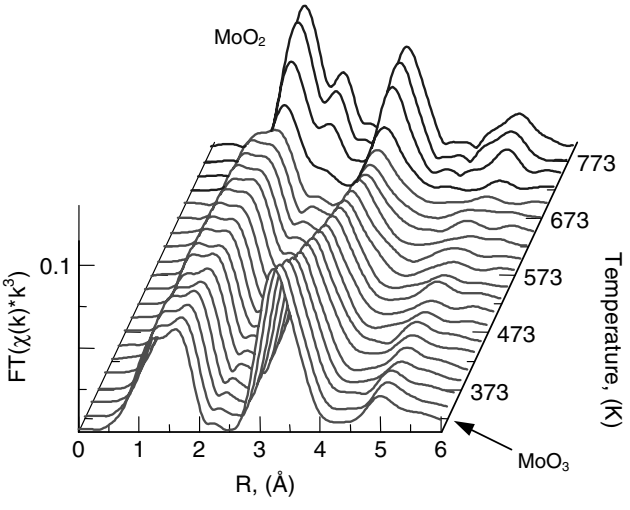

FIG. 7. Evolution of Fourier transformed $\chi(k)$ of the Mo K-edge during TPR of MoO_3 in 10 vol% propene from 300 to 773 K (Fig. 4). The most prominent phases (MoO_2 and MoO_3) are indicated.

In order to obtain a more detailed analysis of the evolution of the MoO_3 structure during TPR in propene, a MoO_3 model structure was refined to the experimental FT($\chi(k)$) shown in Fig. 7 according to the procedure presented above. The good agreement between theory and experiment that can be achieved has been described previously (22, 23). Figure 8 shows the evolution of relative Mo–Mo and Mo–O distances in the MoO_3 structure (Table 2) during TPR of MoO_3 in 10 vol% propene (Fig. 4). As can be seen from Table 2, attempting to refine the MoO_3 model structure to the experimental spectrum of $Mo_{18}O_{52}$ results in characteristic deviations of certain shell distances toward smaller or larger values. In the evolution of selected Mo–O and Mo–Mo distances during TPR of MoO_3 (Fig. 8) similar deviations at temperatures above 573 K can be seen, consistent with the formation of "$Mo_{18}O_{52}$" at this temperature (Fig. 5b).

Isothermal Reduction of MoO_3 with Propene

Principal-component analysis of XANES spectra measured during isothermal reduction of MoO_3 in 5 vol% propene at 698 K yielded three primary components necessary to describe the experimental data. Target transformation of the reference molybdenum oxides shown in Fig. 1 showed MoO_3, MoO_2, and $Mo_{18}O_{52}$ to be suitable references for the three phases found. A least-squares refinement of the sum of the three reference spectra to the

TABLE 2

Coordination Number (CN) and Distance of Mo–O and Mo–Mo Coordination Shells of a MoO_3 Model Structure[a] Obtained from a Refinement of the Model Structure to the Experimental XAFS Functions $\chi(k)$ of MoO_3 and $Mo_{18}O_{52}$[b]

Shell	CN	R_{model} (Å)	R_{MoO3} (Å)	$R_{Mo18O52}$ (Å)	ΔR (Å)
Mo–O	1	1.671	1.665	1.741	**0.076**
Mo–O	1	1.735	1.699	1.700	**0.000**
Mo–O	2	1.948	1.932	1.94	0.008
Mo–O	1	2.251	2.211	2.258	0.047
Mo–O	1	2.332	2.304	2.334	0.03
Mo–Mo	2	3.438	3.445	3.461	**0.016**
Mo–Mo	2	3.696	3.751	3.651	**−0.1**
Mo–Mo	2	3.963	3.963	3.985	0.022

Note. The results described in this paper are bold in the table.

[a] *Pbnm*, $a = 3.936$ Å, $b = 13.855$ Å, $c = 3.696$ Å (46).

[b] $k = 3.1$–15.5 Å^{-1}; $R = 0.8$–4.0 Å; $N_{ind} = 27$; $N_{free} = 13$; eight single-scattering paths and 11 multiple-scattering paths. Parameters refined for MoO_3 are $\Theta(O) = 1252$ K, $\Theta(Mo) = 543$ K, $E_0(Mo) = 7.6$ eV, $E_0(O) = -6.0$ eV (Θ: Debye temperature). The fit residual amounted to 4.6. The differences in distance R for the individual shells for the XAFS refinement to MoO_3 and $Mo_{18}O_{52}$ are given.

experimental spectra resulted in the evolution of the three phases during isothermal reduction at 698 K in 5 vol% propene (Fig. 9). In addition, Fig. 9 shows the normalized ion currents of H_2O, CO_2, and acrolein. It can be seen that the evolution of the products of total and partial oxidation (top of Fig. 9) follows the phase evolution (bottom of Fig. 9). In all of the *in situ* XAFS measurements conducted on the isothermal reduction of MoO_3, the phase concentration of $Mo_{18}O_{52}$ was less than 10%. In the following, the extent of reduction of MoO_3, α, is defined as evolution of the MoO_2 phase during reduction.

Figure 10 shows the extent of reduction α obtained from *in situ* XAFS experiments during isothermal reduction of MoO_3 in 5 vol% propene at 723 K, 10 vol% propene at 673 K, and 10 vol% propene at 698 K. From the α trace at 673 K in 10 vol% propene a deviation from a symmetric sigmoidal trace can be seen. The acceleratory regime of the reduction at 673 K (up to $\alpha \approx 0.3$) can be described by a "power rate law" ($\alpha \sim t^2$) (60), whereas the deceleratory regime of the reduction can be described by a "three-dimensional diffusion" rate law ($\alpha \sim 1-(1-t^{1/2})^3$) (60). The point of change between the two rate laws (i.e., a change in the rate-limiting step) is indicated in Fig. 10. From the isothermal reduction experiments performed it was found that the point of change between the two rate laws is approximately independent of the reaction temperature, but varies with the reactant concentration. As can be seen from Fig. 10, for the reduction of MoO_3 in 10 vol% propene, at both reaction temperatures 673 and 698 K the point of change between a power law and diffusion law is at $\alpha \approx 0.3$. At 723 and 698 K (Fig. 9) in 5 vol% propene, the point of change between the two rate laws is at $\alpha \approx 0.4$ (dotted line in Fig. 10).

The extent of reduction curves obtained for the reduction of MoO_3 in 40 vol% propene at different reaction temperatures (798–648 K) is depicted in Fig. 11a. The nonsymmetric shape of the α traces again indicates a change in the rate-limiting step during reduction of MoO_3. In addition, at reduction temperatures of 798 and 773 K the formation of Mo_4O_{11} distorts the nonsymmetric shape of the extent of reduction traces. Force fitting of the Avrami equation (sigmoidal rate law used to describe nucleation and nuclei growth kinetics) (60) afforded rate constants, which are presented in Fig. 11b in an Arrhenius-type diagram. A linear regression (omitting the rate constant at 648 K) resulted in an apparent activation energy of ~100 kJ/mol. The much smaller rate constant for the reduction at 648 K indicates a change in the rate-limiting step, as a function of the reaction temperature. The extent of reduction trace denoted "Model" in Fig. 11a corresponds to a calculated extent of

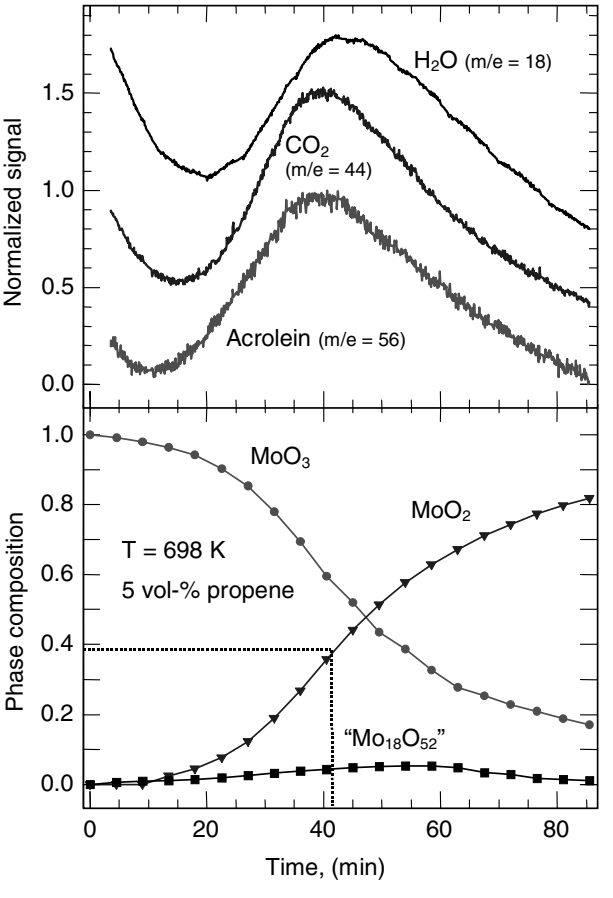

FIG. 9. Evolution of phase composition (MoO_3, MoO_2, $Mo_{18}O_{52}$) (bottom) and normalized concentration of water ($m/e = 18$), CO_2 ($m/e = 44$), and acrolein ($m/e = 56$) in the gas phase during isothermal reduction of MoO_3 in 5 vol% propene at 698 K. Dotted line in bottom part indicates change in rate-limiting step (see Fig. 10).

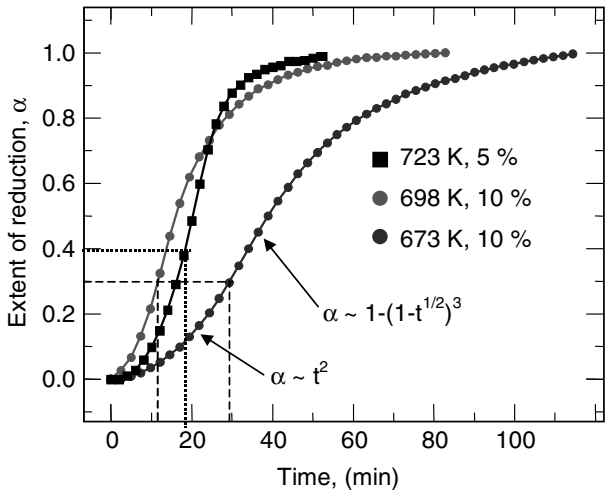

FIG. 10. Extent of reduction α obtained from *in situ* XAFS experiments during isothermal reduction of MoO_3 in 5 vol% propene at 723 K, in 10 vol% propene at 673 K, and in 10 vol% propene at 698 K. The changes in the rate-limiting step from an $\alpha \sim t^2$ rate law (power law) to an $\alpha \sim 1-(1-t^{1/2})^3$ rate law (three-dimensional diffusion) for the experiments at 673 K in 5 vol% ($\alpha \approx 0.30$) and at 723 K in 10 vol% ($\alpha \approx 0.4$) are indicated by a dashed and a dotted line, respectively.

reduction curve assuming the rate constant "Model," as indicated in Fig. 11b.

Evolution of the extent of reduction α during isothermal reduction of MoO_3 in 5 vol% propene at 623, 648, and 673 K obtained from *in situ* XRD experiments is depicted in Fig. 12a. From the half-life normalized traces (inset in Fig. 12a) it can be seen that the same rate laws govern the reduction of MoO_3 at the three temperatures. Figure 12b shows the corresponding apparent activation energy as a function of extent of reduction, $E_a(\alpha)$. The $E_a(\alpha)$ trace was obtained from an isoconversional analysis (39) of the reduction traces in Fig. 12a. It can be seen that the apparent activation energy of the reduction of MoO_3 with propene continuously decreases with increasing extent of reduction α.

For the reduction of MoO_3 in 5 vol% propene at 623 K the evolution of crystallite sizes for directions perpendicular to the (010) and (110) planes in the MoO_3 lattice and for the direction perpendicular to the (011) plane in the MoO_2 lattice as a function of the extent of reduction (Fig. 12a) is depicted in Fig. 13a. Crystallite sizes were calculated from the integral breath of the corresponding diffraction lines of the two structures using the Scherrer formula (40). The dashed line in Fig. 13a indicates the transition from a power law kinetics to a diffusion-controlled regime. From Fig. 13a it can be noticed that in the direction perpendicular to the layers in the MoO_3 structure ([010] direction), a crystallite growth occurs during the reduction of MoO_3 in propene. Unfortunately, diffraction lines from crystallographic planes perpendicular to the MoO_3 layers were not available for analysis. However, from the analysis of the (110) line, which is affected by structural changes in the MoO_3 layers, it can be seen that the (110) diffraction line is broadened during reduction, seemingly resulting in a decrease in crystallite size in the direction perpendicular to (110). MoO_2 crystallites appear to grow rapidly from ~140 to ~170 Å in the early stage of the reduction ($\alpha < 0.4$). For $\alpha > 0.4$ no further growth of the MoO_2 crystallites is observed. It can be seen from Fig. 13a that the point from where on the MoO_2 crystallite size remains constant approximately coincides with the change in rate laws during reduction (dashed line in Fig. 13).

In Fig. 13b the evolution of the lattice constant b of α-MoO_3 and the ratio of integrated intensities (A(020)/

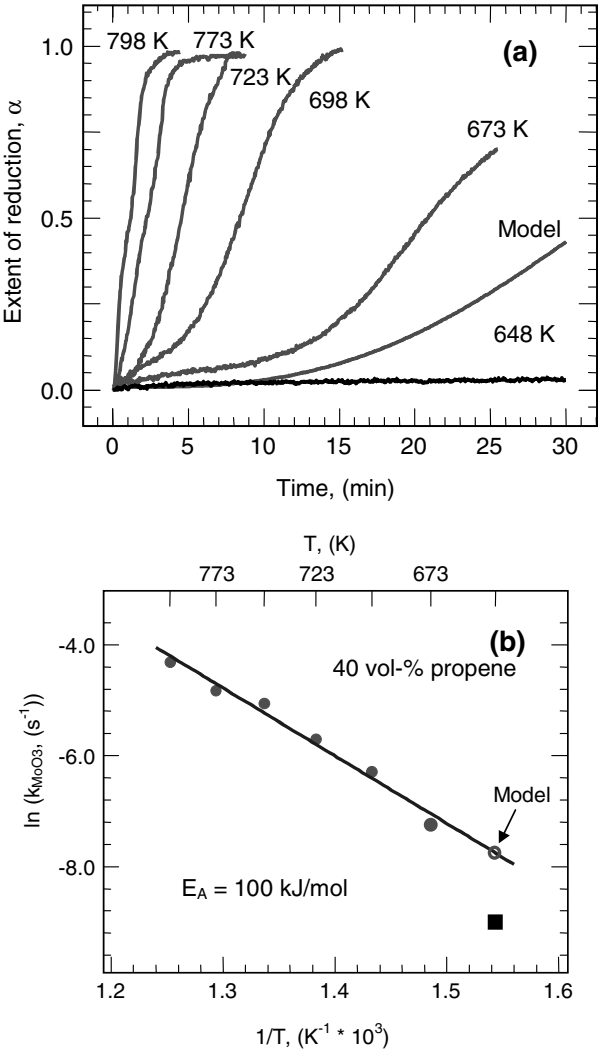

FIG. 11. (a) Extent of reduction α obtained from isothermal *in situ* XAFS experiments at temperatures $T = 798, 773, 723, 698, 673$, and 648 K (square in Fig. 11b) in 40 vol% propene. (b) The trace denoted "Model" (open circle) corresponds to a calculated extent of reduction assuming a rate of reduction in b Arrhenius-type diagram constructed from the rate constants determined for the extent of reduction traces in Fig. 11a. At 673 K a change in the rate-limiting step can be seen.

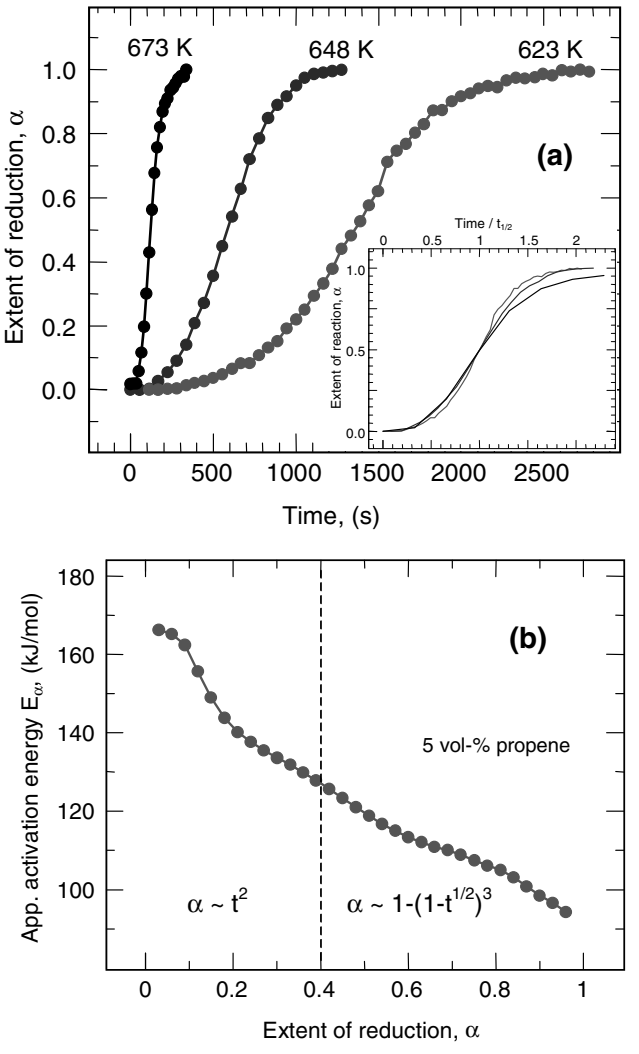

FIG. 12. (a) Evolution of extent of reduction α during isothermal reduction of MoO_3 in 5 vol% propene at 623, 648, and 673 K obtained from *in situ* XRD experiments. The inset shows the corresponding half-life normalized traces. (b) Apparent activation energy as a function of extent of reduction calculated from the reduction traces shown in Fig. 12a.

A(110)) of MoO_3 is depicted during isothermal reduction in 5 vol% propene. It can be seen that the MoO_3 lattice expands slightly in the direction perpendicular to the layers during isothermal reduction in propene. No significant expansion of the MoO_3 lattice in the *a* or *c* direction was observed. Furthermore, from Fig. 13b a considerable increase in the ratio of the integrated intensities A(020)/A(110) for values of α larger than 0.4 can be noticed. The onset of the increase in the ratio of the integrated intensities coincides with the change in the rate laws at $\alpha \approx 0.4$.

Temperature-Programmed Oxidation of MoO_2

The evolution of XRD patterns measured during temperature-programmed oxidation (TPO) of MoO_2 in 20 vol% oxygen from 300 to 773 K at a heating rate of 0.2 K/min exhibited a rapid oxidation of MoO_2 to MoO_3 at ~573 K. No crystalline phases other than MoO_2 and MoO_3 were detected, either under the temperature-programmed or under the isothermal oxidation conditions employed in this work (Table 1). In addition to XRD studies, *in situ* time-resolved XAS experiments were performed during TPO of MoO_2 in oxygen. A principal-component analysis of the XANES spectra measured during TPO of MoO_2 in 5 vol% oxygen from 300 to 773 K at a heating rate of 5 K/min afforded at least three components necessary to describe the experimental data. From target transformation of the molybdenum oxide references in Fig. 1, MoO_2, MoO_3, and $Mo_{18}O_{52}$ were found to be suitable references for the three components observed during oxidation of MoO_2. A least-squares refinement of these three references to the

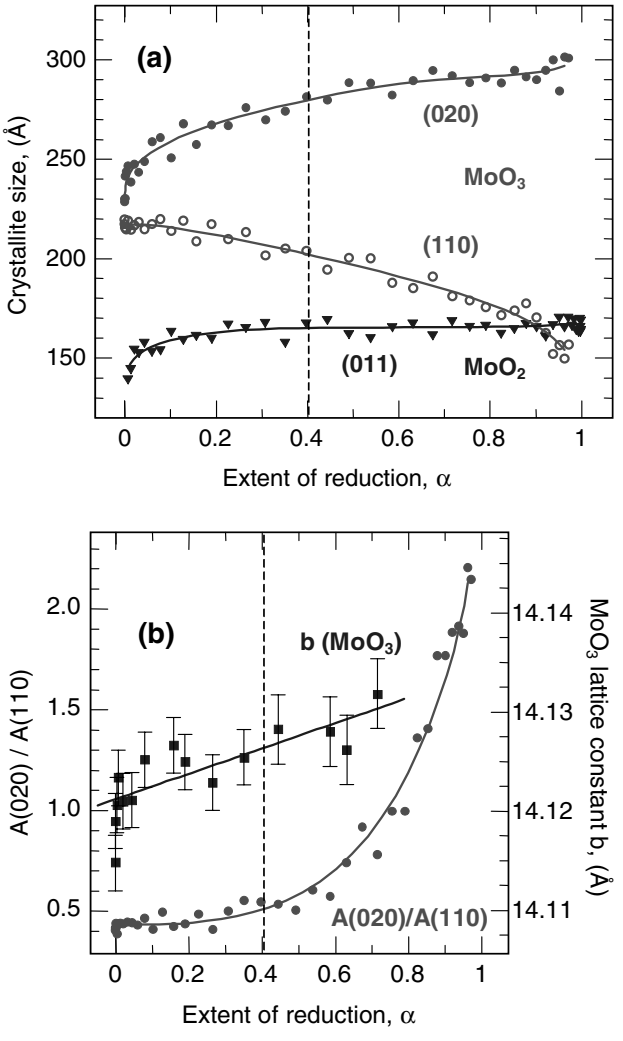

FIG. 13. Evolution of (a) crystallite sizes for different directions in the MoO_3 lattice (circles, (020) and (110)) and the (011) direction in MoO_2 lattice (triangles) and (b) *b* lattice constant of α-MoO_3 (basal plane) and ratio of integrated intensities (A(020)/A(110)) of MoO_3 during reduction of MoO_3 in 5 vol% propene at 623 K. Dashed line indicates the transition from a power law kinetics to a diffusion-controlled regime.

experimental spectra yielded the evolution of the phase composition (MoO_3, MoO_2, $Mo_{18}O_{52}$) during TPO of MoO_2 in 1 vol% oxygen, as depicted in Fig. 14. It can be seen that the oxidation of MoO_2 starts as low as 373 K, whereas rapid and complete oxidation of both MoO_2 and $Mo_{18}O_{52}$ to MoO_3 appears to set in at ~673 K.

Isothermal Oxidation of MoO_2

The isothermal oxidation of MoO_2 was studied by *in situ* XRD at temperatures between 598 and 698 K in 1 vol% oxygen in He (Table 1). At this low oxygen concentration, the oxidation proceeded very rapidly at temperatures above 650 K. Complementary to the *in situ* XRD experiments, *in situ* time-resolved XAS measurements were performed during the isothermal oxidation of MoO_2 in 1 vol% oxygen at temperatures between 673 and 773 K. Half-lives of MoO_2 obtained from *in situ* XRD and XAFS experiments are shown in Fig. 15a. A good agreement in the half-lives obtained with the two techniques can be seen. The inset in Fig. 15a shows the half-life normalized extent of oxidation curves obtained from *in situ* XRD measurements. Because the traces are of similar shape, in the temperature range from 598 to 698 K the oxidation of MoO_2 in 1 vol% oxygen is governed by the same rate law. From an isoconversional analysis of the extent of oxidation traces shown in Fig. 15a, the apparent activation energy as a function of the extent of oxidation α, $E_a(\alpha)$, was calculated (Fig. 15b). For the oxidation of MoO_2 in 1 vol% oxygen, it can be seen that the apparent activation energy increases continuously during the reaction, ranging from ~95 to ~180 kJ/mol.

A principal-component analysis of the Mo *K* near-edge spectra measured during isothermal oxidation of MoO_2 in

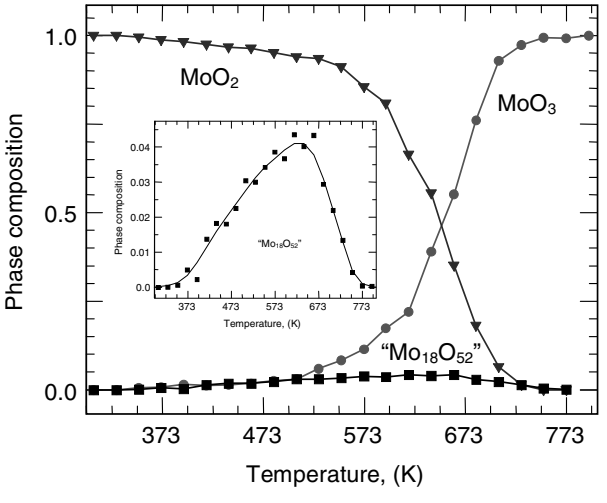

FIG. 14. Evolution of phase composition (MoO_3, MoO_2, $Mo_{18}O_{52}$) during TPO of MoO_2 in 5 vol% oxygen from 300 to 773 K at a heating rate of 5 K/min obtained from an *in situ* XAFS experiment. Inset shows an enlargement of the evolution of $Mo_{18}O_{52}$.

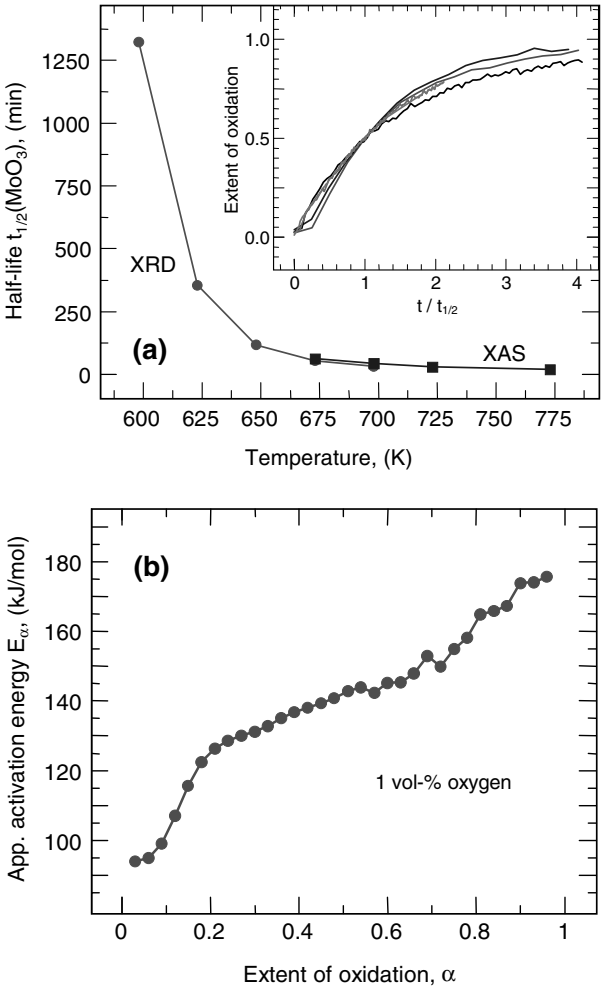

FIG. 15. (a) Half-life of MoO_2 as a function of temperature obtained from *in situ* XRD and *in situ* XAFS measurements during isothermal oxidation of MoO_2 in 1 vol% oxygen. The inset shows the half-life normalized extent of oxidation traces from *in situ* XRD experiments at the corresponding temperatures. (b) Apparent activation energy as a function of extent of oxidation calculated from the extent of oxidation traces shown in Fig. 15a.

1 vol% oxygen at temperatures above 673 K afforded the two majority phases, MoO_2 and MoO_3, and the minority phase, $Mo_{18}O_{52}$, to be sufficient to describe the experimental data. It is interesting that PCA of XANES spectra measured for 60 min during oxidation of MoO_2 at 673 K yielded only two phases necessary to describe the experimental data, namely MoO_2 and $Mo_{18}O_{52}$. Only after reaction times of more than 60 min was MoO_3 detected as a third phase.

DISCUSSION

Structural Evolution during Reduction of MoO_3 in Propene

In the work presented here the reduction of the layer structure of orthorhombic MoO_3 (*Pbnm*, $a = 3.936$ Å,

$b = 13.855$ Å, $c = 3.696$ Å) with propene and the oxidation of the rutile structure of MoO_2 with oxygen have been studied under various reactant concentrations in temperature-programmed and isothermal experiments (Table 1). Reduction and reoxidation of MoO_{3-x} are of particular interest because they constitute the two fundamental steps of the so-called redox mechanism for partial oxidation of alkenes on molybdenum oxide catalysts (1). During temperature-programmed reduction of MoO_3 with propene no crystalline phases other than MoO_3 and MoO_2 were detected by *in situ* XRD (Fig. 2). However, during TPR in propene two distinct peaks in the evolution of the gas-phase concentration of H_2O, CO_2, and acrolein were seen (Fig. 5a), whereas during TPR in hydrogen only one distinct peak in the evolution of H_2O was observed (data from Ref. 23). The two peaks observed in the evolution of the gas-phase composition together with the corresponding two peaks in the first derivative of the Mo *K*-edge shift indicate the presence of an intermediate phase during reduction of MoO_3 in propene. Principal-component analysis of XANES spectra measured during TPR of MoO_3 in propene identified this intermediate as $Mo_{18}O_{52}$ (Fig. 5b). Because the mass spectrometer used for the XRD and XAS experiments was not calibrated, only qualitative catalysis data can be provided. However, at 713 K the conversion of propene on MoO_3 was reported to be 7% with an acrolein yield of 2% (5), and it is assumed that the catalytic behavior of the material used here is similar. In addition to the TPR experiments, the formation of $Mo_{18}O_{52}$ was also observed during isothermal reduction of MoO_3 at the temperatures employed.

To further corroborate the formation of $Mo_{18}O_{52}$ a detailed EXAFS analysis of the Fourier transformed $\chi(k)$ (Fig. 7) measured during TPR of MoO_3 in propene was performed. By using theoretical phases and amplitudes calculated for the orthorhombic layer structure of MoO_3, an excellent agreement between theory and experiment can be achieved. However, with increasing reaction temperature a mixture of up to three phases (MoO_3, $Mo_{18}O_{52}$, and MoO_2) is obtained that cannot be fitted anymore by a mixture of the EXAFS functions of the three different model systems in spite of the good data quality of the $\chi(k)$ up to ~16 Å (Fig. 6). Therefore, an EXAFS fit of a single MoO_3 model structure to the experimental $\chi(k)$ measured was attempted up to temperatures of 673 K (i.e., formation of MoO_2). From Table 2 it can be seen that trying to refine the MoO_3 model structure to an experimental $\chi(k)$ of the reference $Mo_{18}O_{52}$ results in characteristic changes in certain Mo–O and Mo–Mo bond distances. From Fig. 8 it can be noticed that at a reaction temperature of about 573 K significant changes in nearest-neighbor distances occur that coincide with the onset of the formation of $Mo_{18}O_{52}$ (Fig. 5b) and that are in agreement with the deviations expected when trying to fit a MoO_3 model structure to an experimental $\chi(k)$ of $Mo_{18}O_{52}$ (Table 2).

According to the XANES (Fig. 5b) and the EXAFS analysis (Fig. 8), $Mo_{18}O_{52}$ indeed appears to be an intermediate of the reduction of MoO_3 to MoO_2 in propene. Because under no reaction conditions were crystalline phases other than MoO_3 and MoO_2 detected by *in situ* XRD, the intermediate phase shown in Fig. 5b is denoted $Mo_{18}O_{52}$. This is meant to indicate that we are not referring to a crystalline $Mo_{18}O_{52}$ intermediate phase but to a highly disordered partially reduced MoO_3 that contains a number of crystallographic-shear (CS) planes similar to those in $Mo_{18}O_{52}$ and that exhibit a Mo *K* near-edge spectrum similar to that of crystalline $Mo_{18}O_{52}$.

The formation of $Mo_{18}O_{52}$ and, hence, of CS planes during the reduction of MoO_3 with propene is in good agreement with previous studies (41, 42), in particular with the direct observation of the formation of CS planes by electron microscopy (12). In addition, theoretical calculations have shown that the removal of oxygen from the lattice is facilitated when accompanied by a structural rearrangement of the oxide lattice resulting in crystallographic shear (43, 44). However, an equilibrium should exist between CS structures and point defects that may explain the reactivity observed for ReO_3-type oxides (45). MoO_3 is known to form a number of suboxides with average valences between 6.0 and 5.5 (e.g., MoO_3 (46), $Mo_{18}O_{52}$ (47), Mo_8O_{23} (48), Mo_4O_{11}, (49)). Several of the molybdenum suboxides form different types of shear structures and the origin of CS planes in MoO_3 was described in detail by Bursill (50). With respect to the molybdenum oxide references (Fig. 1) employed in the principal-component analysis of the *in situ* XANES spectra (Fig. 4), only $Mo_{18}O_{52}$ ($P-1$, $a = 8.145$ Å, $b = 11.890$ Å, $c = 21.230$ Å, $\alpha = 102.7°$, $\beta = 67.8°$, $\gamma = 110.0°$) was identified as a probable intermediate phase during the reduction of MoO_3 in propene. Other suboxides that also contain CS planes (e.g., Mo_8O_{23}) were not detected during the reduction.

The structures of two molybdenum suboxides that contain CS planes, i.e., $Mo_{18}O_{52}$ and Mo_8O_{23}, can be derived by crystallographic-shear operations. CS transforms a subset of octahedra along specific planes from a corner-sharing to an edge-sharing arrangement. While the $Mo_{18}O_{52}$ structure is derived from the α-MoO_3 structure, the Mo_8O_{23} structure is derived from the ReO_3 structure. Thus, Mo_8O_{23} is a three-dimensionally bonded structure that does not contain a van der Waals gap like those of MoO_3 and $Mo_{18}O_{52}$ (51). Given these considerations, the formation of a α-MoO_3-type shear structure ($Mo_{18}O_{52}$) during reduction of MoO_3 in propene appears much more likely than the formation of a ReO_3-based shear structure (Mo_8O_{23} (52) or Mo_4O_{11} (53)), which would require a considerable reconstructive structural transformation.

For the reduction of MoO_3 with propene we propose the following reaction mechanism (schematic representation shown in Fig. 16, left side). Oxidation of propene with

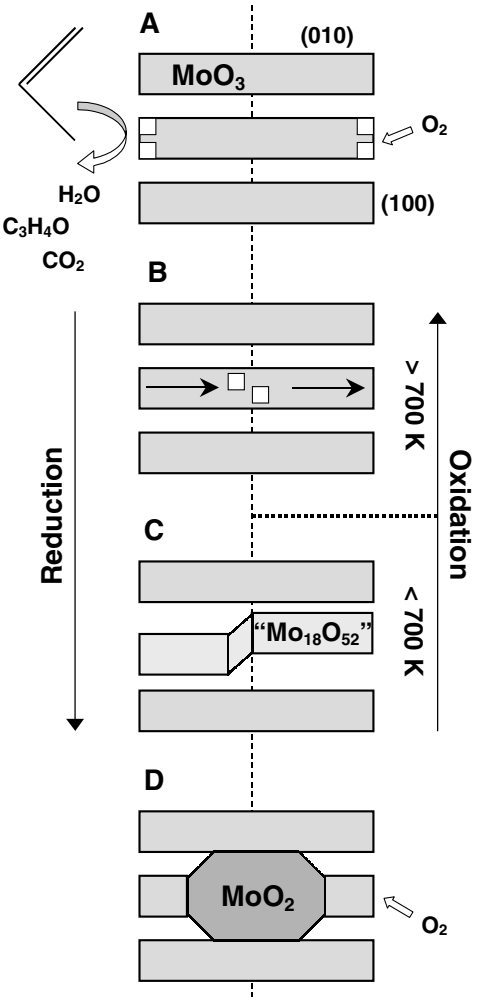

FIG. 16. Schematic representation of a mechanism for the reduction of MoO_3 with propene to MoO_2. (A) Oxidation of propene with lattice oxygen at the (100) or (001) facets of MoO_3 and formation of oxygen vacancies. (B) Diffusion of oxygen vacancies into the MoO_3 bulk along [100] or [001]. (C) Consumption of oxygen vacancies by formation of shear structures ($Mo_{18}O_{52}$) in the MoO_3 bulk. (D) Nucleation and subsequent growth of MoO_2.

lattice oxygen takes place at the (100) or (001) facets of MoO_3 and results in the formation of oxygen vacancies (Fig. 16A). By means of oxygen vacancy diffusion into the MoO_3 bulk along the [100] or [001] direction, lattice oxygen at the surface of the (100) or (001) facets is replenished (Fig. 16B). Because oxygen diffusion in the MoO_3 layer structure along [100] or [001] is much faster than along [010] (perpendicular to the layers) (16, 54, 55), generation of oxygen vacancies at the basal planes of MoO_3 does not play a significant role in the bulk reduction of MoO_3 in propene. After a certain concentration of oxygen vacancies in the MoO_3 bulk structure has been exceeded, the oxygen vacancies are consumed by the formation of shear structures ($Mo_{18}O_{52}$ type) in the MoO_3 bulk (Fig. 16C). Eventually, the shear structures serve as nucleation sites for the formation and subsequent growth of MoO_2 crystallites (Fig. 16D). The overall mechanism is in good agreement with individual steps that have been previously proposed (11, 56, 57).

The schematic model in Fig. 16 is further corroborated by the evolution of the MoO_3 structure obtained from isothermal XRD experiments during reduction with propene. Figure 13b shows a slight increase in the *b* lattice constant of MoO_3 during reduction that corresponds to an expansion of the structure perpendicular to the layers. This expansion is probably caused by the formation of $Mo_{18}O_{52}$ type shear structures in the MoO_3 bulk (Fig. 16C). A similar expansion has been reported for the mechanical activation of MoO_3 (58). During temperature-programmed reduction this expansion was obscured by the large thermal expansion of MoO_3 in the *b* direction (Fig. 3); however, it is clearly detectable during isothermal reduction. It can also be seen from Fig. 13b that the ratio of the integrated intensities (peak area) of the (020) and (110) diffraction line of MoO_3 increases during reduction in propene. This increase in the A(020)/A(110) ratio indicates that diffraction by the (110) lattice planes that contain contributions from the in-plane structure of MoO_3 is more affected by the ongoing reduction than is diffraction by the (020) lattice planes that correspond to the stacking of the layers in the MoO_3 structure. It can be imagined from Fig. 16C that the formation of shear structures in the MoO_3 lattice and the subsequent growth of MoO_2 nuclei has a more pronounced effect on diffraction from the in-plane structure than from the layer structure of MoO_3. Similarly, the evolution of the MoO_3 crystallite sizes calculated from the (110) and (020) diffraction line width indicates an anisotropic structural change in the MoO_3 lattice during reduction in propene (Fig. 13a) (59).

Solid-State Kinetics of the Reduction of MoO_3 in Propene

In addition to the evolution of phases (Fig. 9) and the bulk structure of MoO_3 (Fig. 13) during the reduction in propene, the solid-state kinetics of the reduction of MoO_3 was obtained from isothermal time-resolved XRD and XAFS experiments at various temperatures and under different reactant concentrations (Table 1). It was found that the extent of reduction curves obtained (Figs. 10–12) could not be sufficiently described by a single rate law. This indicates that the kinetics of the reduction of MoO_3 with propene is governed by at least two different rate-determining steps. The half-life normalized traces shown in Fig. 12a (inset) indicate that the contribution of the two separate rate laws to the overall extent of reduction curves remains approximately the same at different reaction temperatures.

From the various solid-state kinetic models described in the literature (60–62) the following two rate laws were found to yield the best agreement with the experimental data (Fig. 10). During the first stage of the reduction (up to

$\alpha = 0.3$ in 10 vol% propene) the rate of reduction is best described by a "power law," $\alpha = kt^2$. Provided a rapid ("instantaneous") nucleation is assumed to occur in the very early stage of the reduction, the power law indicates a growth of the MoO_2 nuclei in two dimensions in the MoO_3 layer structure. The growth of the MoO_2 crystallites formed during the first stage of the reduction of MoO_3 can indeed be seen in the evolution of crystallite sizes obtained from isothermal *in situ* XRD measurements (Fig. 13a). In addition, the very rapid nucleation process may be the reason for the rapid increase in the *b* lattice constant of MoO_3 in the very early stage of the reduction with propene (Fig. 13b).

With increasing extent of reduction α the rate law changes from a power law to a rate law that indicates that diffusion in three dimensions is the rate-determining step ($\alpha \sim 1 - (1 - t^{1/2})^3$) (Fig. 10). During this second stage of the reduction, the MoO_2 nuclei that have formed in the first stage of the reduction are growing in three dimensions in the MoO_3 layer structure, with mass diffusion in the three dimensions being the rate-determining step. It is interesting that the "crossover point" in α where the power law kinetic changes to a diffusion-controlled kinetic varies with increasing propene concentration. It is found that the crossover point shifts toward smaller values of α with increasing propene concentration. This indicates that with increasing propene concentration and, hence, increasing reduction rate, diffusion in the MoO_3 crystallites becomes rate limiting sooner than at lower propene concentrations at the same temperature. This can be seen for the reduction at 698 K in 10 vol% propene, which proceeds initially faster than the reduction at 723 K in 5 vol% propene (Fig. 10). However, for the reduction at 698 K in 10 vol% propene the crossover point is $\alpha \approx 0.3$, whereas at 723 K in 5 vol% the crossover point is $\alpha \approx 0.4$.

In addition to a change in the rate-limiting step as a function of the extent of reduction (Fig. 10), a change in the rate-limiting step was also observed with decreasing reaction temperature. From the extent of reduction curves depicted in Fig. 11a for the reduction of MoO_3 in 40 vol% propene it can be seen that at a reaction temperature of 648 K the extent of reduction curve can not be described anymore by a "nucleation-growth" rate law (as indicated by the discrepancy between the trace labeled "Model" in Fig. 11 and the corresponding experimental trace at 648 K). Instead, the extent of reduction curve in 40 vol% propene at 648 K has to be described as being entirely diffusion controlled. The temperature of 648 K coincides with a change in the rate-limiting step for $\alpha > 0.5$ from "nuclei growth" to "diffusion control" observed for the oxidation of MoO_2 in 100 vol% oxygen (24). Apparently, at this reaction temperature in 40 vol% propene the diffusion of oxygen in the layers of MoO_3 (Fig. 16B) is not sufficient anymore to permit fast enough nuclei formation and nuclei growth.

By "force fitting" the Avrami equation to the extent of reduction curves depicted in Fig. 11a, rate constants were obtained and subsequently used to assemble the Arrhenius-type diagram shown in Fig. 11b. The apparent activation energy obtained (~100 kJ/mol) is in good agreement with values reported in the literature (11, 17, 63) and the isoconversional analysis as described below. Furthermore, it can be seen from the change in slope in the extent of reduction curves at 798 and 773 K that at these temperatures the formation of Mo_4O_{11} was observed from a parallel reaction of MoO_2 and MoO_3 (25).

Because the overall shape of the extent of reduction curves obtained from isothermal XAS and XRD experiments is not significantly affected by the reaction temperature (Fig. 12a), isoconversional analyses (39) of sets of the extent of reduction curves obtained at different temperatures under the same reactant concentration were performed. In the conventional "model force fitting" analysis of solid-state kinetic data, a "suitable" solid-state kinetic model is refined to the experimental extent of reaction curves and the apparent activation energy is obtained from an Arrhenius-type diagram (Fig. 11b). In contrast, from an isoconversional analysis the evolution of the apparent activation energy as a function of the proceeding solid-state reaction can be obtained on a model-free basis. In Fig. 12b the evolution of the apparent activation energy $E_a(\alpha)$ as a function of the extent of reduction α is depicted for the reduction of MoO_3 in 5 vol% propene (Fig. 12a). It can be seen that $E_a(\alpha)$ decreases from ~160 kJ/mol in the stage of reduction that is governed by MoO_2 nucleation and growth in two dimensions (power law, $\alpha \sim t^2$) to ~100 kJ/mol in the stage of reduction that is controlled by diffusion in three dimensions. This range is in good agreement with the previously reported apparent activation energies for oxygen vacancy diffusion in MoO_3 of about 93 kJ/mol (11, 63). Also the apparent activation energy of 120 kJ/mol, as proposed by Abon *et al.* (17) for the partial oxidation of propene to acrolein, lies well within the range given in Fig. 12.

Because an isoconversional analysis of isothermal reduction curves is a model-free approach, by definition it does not permit conclusions regarding the reaction mechanism. However, empirically it has been found that certain $E_a(\alpha)$ curves are often associated with particular reaction mechanisms. A decreasing apparent activation energy as a function of α, as shown in Fig. 12b, for instance, may indicate a reaction that is complicated by diffusion (39) which would be in good agreement with the model-based analysis of the isothermal extent of reduction curves (Fig. 9).

The solid-state kinetics of the reduction of MoO_3 in propene as obtained from isothermal *in situ* XRD and XAS experiments corroborates the reduction model proposed in Fig. 16. In the early stage of the reduction ($\alpha < 0.3$) the steps A (formation of oxygen vacancies), B (vacancy diffusion), C

(formation of shear-structures $Mo_{18}O_{52}$), and D (formation of MoO_2 nuclei in the MoO_3 layer structure) proceed very rapidly, resulting in the observed power law ($\alpha \sim t^2$) (Fig. 10). With increasing extent of reduction, the MoO_2 nuclei formed need to grow in three dimensions, which is rendered difficult by the lack of diffusion paths across the van der Walls gap perpendicular to the layers in MoO_3. In this stage of the reduction of MoO_3 with propene, mass diffusion in three dimensions in the MoO_3 bulk becomes rate limiting.

Reduction of MoO_3 in Propene or Hydrogen

In contrast to the reduction of MoO_3 in hydrogen (23), no formation of molybdenum bronzes was observed during reduction of MoO_3 in propene. Apparently, during reduction in propene, hydrogen is not at all or only to a small extent incorporated into the MoO_3 layer structure. Similar to the reduction of MoO_3 with hydrogen, no formation of Mo_4O_{11} was detected under temperature-programmed conditions. During isothermal reduction of MoO_3 with propene at temperatures above 750 K, however, the formation of Mo_4O_{11} was detected. This observation corroborates our previous conclusion that Mo_4O_{11} is formed from a parallel reaction of MoO_3 and MoO_2 and is not an intermediate of the reduction of MoO_3 (25).

Compared to the solid-state kinetics of the reduction of MoO_3 in hydrogen several significant differences were found in the kinetics of the reduction of MoO_3 in propene. Although in both cases the early stage of the reduction is governed by product nucleation and nuclei growth, a $\alpha \sim t^3$ rate law was found for the reduction in hydrogen (25), whereas a $\alpha \sim t^2$ rate law is found for the reduction in propene. Assuming the same very rapid nucleation in the very early stage of the reduction, the former indicates a growth in three dimensions, whereas for the reduction in propene the growth of the product nuclei is confined to two dimensions in the MoO_3 layer structure. Furthermore, the strong dependence of the apparent activation energy on the reactant concentration that was found for the reduction of MoO_3 in hydrogen (25) was not observed for the reduction in propene. Apparently, the incorporation of hydrogen in the MoO_3 layer structure during reduction (23) results in a lowering of the apparent activation energy with increasing hydrogen concentration. Because no detectable amount of hydrogen is incorporated in the MoO_3 structure during reduction in propene, the apparent activation energy for the processes occurring in the MoO_3 bulk during nucleation and nuclei growth remain basically unaffected by the propene concentration. Different apparent activation energies for the reduction of MoO_3 with hydrogen and propene have been previously reported and attributed to the different energies required for the dissoziative adsorption of H_2 and propene on MoO_3 (53, 64). In contrast to the results described above, Sloczynski and co-workers proposed an autocatalytic mechanism for the reduction of MoO_3 in the temperature range 733–813 K with the same kinetics and rate-determining step in both hydrogen and propene (53, 65). However, at these temperatures, addition of MoO_2 results in the formation of Mo_4O_{11} and, thus, naturally alters the reduction properties of the system studied. Conversely, in our studies, no effect of adding MoO_2 on the rate of reduction was observed at temperatures below 700 K. Furthermore, the results outlined above clearly indicate different kinetics for the reduction of MoO_3 in hydrogen and propene.

Structural Evolution during Oxidation of MoO_2 in Oxygen

Similar to the reduction of MoO_3 with propene, MoO_3 and MoO_2 were the only crystalline phases detected by *in situ* XRD during temperature-programmed or isothermal oxidation of MoO_2 to MoO_3 (Fig. 15a). However, principal-component analysis of XANES spectra measured during TPO of MoO_2 clearly indicated the presence of at least three components necessary to reconstruct the experimental data. When the XANES spectra of the molybdenum oxide references were employed, as shown in Fig. 1, only $Mo_{18}O_{52}$ was found to be a suitable reference compound in addition to MoO_2 and MoO_3. Because no crystalline $Mo_{18}O_{52}$ was detected by *in situ* XRD, the intermediate phase in the oxidation of MoO_2 to MoO_3 is denoted $Mo_{18}O_{52}$. Similarly to the reduction of MoO_3 in propene, $Mo_{18}O_{52}$ refers to a disordered MoO_3 that contains a large number of CS planes similar to those in $Mo_{18}O_{52}$ and that exhibits a Mo K near-edge spectrum similar to that of crystalline $Mo_{18}O_{52}$. Most likely the $Mo_{18}O_{52}$ phase detected during oxidation of MoO_2 is identical to that observed during the reduction of MoO_3 in propene.

The evolution of the three phases (MoO_2, MoO_3, and $Mo_{18}O_{52}$) during TPO of MoO_2 is depicted in Fig. 14. It can be seen that the oxidation of MoO_2 and the formation of $Mo_{18}O_{52}$ already starts at a temperature as low as 373 K, although no changes in the diffraction patterns (lattice parameters or crystallite size) are detectable at this temperature. At temperatures above 573 K a rapid increase in the concentration of MoO_3 can be seen (Fig. 14) accompanied by a decrease in the concentration of $Mo_{18}O_{52}$. In addition to the TPO of MoO_2, the formation of $Mo_{18}O_{52}$ was also observed during isothermal oxidation of MoO_2. It is interesting that at temperatures below 673 K in 1 vol% oxygen, MoO_2 and $Mo_{18}O_{52}$ are the two majority phases detected by *in situ* XAFS. Only after more than 60 min at 673 K, a slow increase in the concentration of MoO_3 can be noticed. At an oxidation temperature of 723 K the two majority phases detected are MoO_2 and MoO_3, whereas $Mo_{18}O_{52}$ is observed as a minority phase only. Apparently, the short-range-order structure of the oxidation product at 673 K contains at least some of the structural features of $Mo_{18}O_{52}$, leading, for instance, to the shift in the imaginary part of the FT($\chi(k)$)

toward higher distances. This is in agreement with the assumption that $Mo_{18}O_{52}$ corresponds to a disordered MoO_3 with a number of CS planes in the layer structure. At temperatures above 700 K $Mo_{18}O_{52}$ is an intermediate of the oxidation of MoO_2 to MoO_3, whereas at temperatures below 700 K $Mo_{18}O_{52}$ seems to be the product of the oxidation of MoO_2 in oxygen.

Apparently, $Mo_{18}O_{52}$ is an intermediate in both the reduction of MoO_3 in propene and the oxidation of MoO_2 in oxygen. Given the general suitability of $Mo_{18}O_{52}$ as an intermediate structure for the transformation of MoO_3 to MoO_2, it appears likely that a similar structural transformation is also operative in the reduction of MoO_3 with hydrogen. However, apparently the presence of hydrogen in the MoO_3 structure strongly affects the solid-state kinetics of the reduction and prevents the detection of significant amounts of a $Mo_{18}O_{52}$ intermediate by *in situ* XRD and XAS (25).

A schematic representation of a reaction mechanism for the oxidation of MoO_2 in oxygen is depicted in Fig. 16 (right side). In the early stage of the oxidation (Fig. 16D) the rutile structure of MoO_2 is transformed into the layer structure of MoO_3, which at this stage, though, still contains a large number of CS planes (Fig. 16C). At temperatures below 700 K, it seems that the presence of CS planes in MoO_3 does not improve oxygen diffusion in the lattice, as suggested previously (66). At reaction temperatures above ~700 K (Fig. 16B) the generation of oxygen vacancies from the $Mo_{18}O_{52}$-type shear structures and diffusion of the vacancies to the (100) or (001) surfaces of MoO_3 is sufficiently fast to permit complete oxidation to MoO_3 (Fig. 16A). The overall mechanism proposed in Fig. 16 is in agreement with previous reports on the oxidation of MoO_2 or $Mo_{18}O_{52}$. (42, 67–69).

Solid-State Kinetics of the Oxidation of MoO_2 with Oxygen

The solid-state kinetic of the oxidation of MoO_2 in 100 vol% oxygen has been described in detail in a previous study (24). The half-life of MoO_2 during oxidation in 1 vol% oxygen as a function of reaction temperature obtained from isothermal *in situ* XRD and XAS measurements is shown in Fig. 15a. In the overlapping temperature region at 675 and 700 K the good agreement in the half-lives as determined by the two techniques can be seen. The half-life normalized extent of oxidation traces depicted in Fig. 15a indicate that over the temperature range studied approximately the same rate law governs the oxidation of MoO_2 in 1 vol% oxygen. A rate law that assumes diffusion in three dimensions to be the rate-limiting step ($\alpha \sim 1 - (1 - t^{1/2})^3$) was again found to yield the best match to the experimental extent of oxidation traces. The evolution of the apparent activation energy as a function of the extent of oxidation, $E_a(\alpha)$ (Fig. 15b), in 1 vol% oxygen was obtained from an isoconversional analysis of the extent of oxidation curves corresponding that shown in Fig. 15a. In contrast to the reduction of MoO_3 with propene, an increase in $E_a(\alpha)$ with α was obtained for the oxidation of MoO_2 ranging from ~100 to ~180 kJ/mol. This range is in good agreement with a previously reported apparent activation energy of 148 kJ/mol obtained by model force fitting (24, 70, 71). Empirically it was found that an increasing $E_a(\alpha)$ trace may be indicative of a consecutive reaction (39) which is in agreement with the mechanism depicted in Fig. 16.

Compared to the solid-state kinetics observed for the oxidation of MoO_2 in 100 vol% oxygen (24), a transition in kinetics seems to occur as a function of the oxygen concentration. Apparently, at high oxygen concentrations the mass transport of oxygen in the MoO_2 bulk is not rate limiting in the early stage of the oxidation. However, it becomes rate limiting with increasing α and at temperatures below 700 K (24). At low oxygen concentrations the mass transport of oxygen is rate limiting throughout the entire oxidation of MoO_2 to MoO_3, although with a varying apparent activation energy as a function of the extent of oxidation.

Implications of Phase and Structural Evolution during Reduction and Oxidation of MoO_{3-x} for Partial Oxidation Reactions

Combining the results obtained on the structural evolution and the solid-state kinetics of the reduction of MoO_3 in propene and the oxidation of MoO_2 in oxygen, three different temperature-dependent stages of the partial oxidation of propene with oxygen on MoO_3 are suggested. At temperatures below ~600 K the diffusion of oxygen vacancies in the layers of the MoO_3 structure is too slow to permit any considerable contribution of bulk oxygen to the partial oxidation reaction. Any reaction occurring in this temperature regime proceeds by oxygen species adsorbed on the surface of MoO_3 or by participation of oxygen in only the topmost surface layers of the MoO_3 structure (72).

At temperatures between ~600 and ~700 K the rate of diffusion of oxygen in the MoO_3 bulk is sufficient to permit participation of bulk oxygen in the oxidation of propene at the (100) or (001) side planes of the MoO_3 structure (Fig. 16). Propene oxidation products obtained indicate that both partial and total oxidation proceed on the (100) and (001) facets of MoO_3. Reoxidation of the MoO_{3-x} bulk by oxygen from the gas phase will not remove the shear structures formed in the MoO_3 structure ($Mo_{18}O_{52}$). This explains the average valence of less than 6.0 that has been reported in the literature for MoO_3 catalysts under reaction conditions.

At reaction temperatures above ~700 K the formation of oxygen vacancies from the shear structures in the MoO_3 lattice is facilitated, and given the rapid diffusion of these vacancies in this temperature regime, a complete reoxidation of the catalyst with oxygen from the gas phase is feasible.

Apparently, in the second and the third stage described, a redox mechanism for partial oxidation of propene on MoO_3 involving the participation of bulk oxygen may be operative.

CONCLUSIONS

Reduction of MoO_3 in propene and oxidation of MoO_2 in oxygen were investigated by *in situ* XRD and XAFS. Temperature-programmed and isothermal experiments were performed to elucidate the structural evolution of phases present during the reactions and, in addition, to reveal the solid-state kinetics of the processes involved. During the reduction of MoO_3 in propene and the oxidation of MoO_2, only crystalline MoO_3 and MoO_2 were detected by *in situ* XRD. However, analysis of the *in situ* XAFS data yielded the formation of $Mo_{18}O_{52}$-type shear structures as intermediate of both the reduction of MoO_3 in propene and the oxidation of MoO_2 in oxygen. At temperatures below ~700 K oxidation of MoO_2 afforded a disordered MoO_3, with $Mo_{18}O_{52}$-type shear structures in the lattice. Only at temperatures above ~700 K was complete oxidation to MoO_3 observed.

The solid-state kinetics of the reduction of MoO_3 in propene exhibits a change in the rate-limiting step both as a function of temperature and as a function of the extent of reduction α. With increasing α at a given temperature a transition from nuclei growth kinetics to a three-dimensional diffusion-controlled regime is observed. With decreasing temperature (<600 K) a transition to a regime that is entirely controlled by oxygen diffusion in the MoO_3 lattice was found. The solid-state kinetics of the oxidation of MoO_2 is governed by three-dimensional diffusion.

A schematic reaction mechanism for the reduction of MoO_3 in propene and the reoxidation in oxygen is proposed that consists of (i) generation of oxygen vacancies at the (100) or (001) facets by reaction with propene, (ii) vacancy diffusion in the MoO_3 bulk, (iii) formation of $Mo_{18}O_{52}$-type shear structures in the lattice, and (iv) formation and growth of MoO_2 nuclei. The mechanism is in agreement with previous reports of the propene oxidation on MoO_3 being a structure-sensitive reaction.

With respect to a redox mechanism for the partial oxidation of propene on MoO_3, three stages are distinguished. (i) At temperatures below ~600 K the participation of oxygen from the MoO_3 bulk is negligible. (ii) At temperatures between ~600 and ~700 K oxygen vacancy diffusion in the bulk is sufficient to make a redox mechanism feasible. Because the complete reoxidation of the $Mo_{18}O_{52}$-type shear structures is inhibited, a partially reduced MoO_3 with CS planes in the lattice is obtained under reaction conditions. (iii) At temperatures above ~700 K sufficiently fast oxygen diffusion in the lattice combined with rapid formation and annihilation of CS permits the participation of a considerable amount of the lattice oxygen of MoO_3 in the partial oxidation of propene.

ACKNOWLEDGMENTS

The synchrotron radiation facilities HASYLAB, Hamburg, Germany, and ESRF, Grenoble, France, are acknowledged for providing beamtime for this work. TR thanks the Deutsche Forschungsgemeinschaft, DFG, for financial support (Habilitationsstipendium). The authors are particularly grateful to A. Blume for preparing the molybdenum oxide references. O. Timpe and F. Girgsdies are acknowledged for participating in the XAFS measurements. Finally the authors are indebted to Prof. R. Schlögl for many fruitful discussions and continuous support.

REFERENCES

1. Grzybowska-Swierkosz, B., *Top. Catal.* **11/12**, 23 (2000).
2. Grasselli, R. K., *Catal. Today* **49**, 141 (1999).
3. Haber, J., and Lalik, E., *Catal. Today* **33**, 119 (1997).
4. Bettahar, M. M., Costentin, G., Savary, L., and Lavalley, J. C., *Appl. Catal. A* **145**, 1 (1996).
5. Grzybowska, B., Haber, J., and Janas, J., *J. Catal.* **49**, 150 (1977).
6. Brückmann, K., Grabowski, R., Haber, J., Mazurkiewicz, A., Sloczynski, J., and Wiltowski, T., *J. Catal.* **104**, 71 (1987).
7. Mars, P., and van Krevelen, D. W., *Chem. Ing. Sci.* **3**, 41 (1954).
8. Novakova, J., *Catal. Rev.* **4**, 77 (1971).
9. Krenzke, L. D., and Keulks, G. W., *J. Catal.* **61**, 316 (1980).
10. Ueda, W., Moro-Oka, Y., and Ikawa, T., *J. Catal.* **70**, 409 (1981).
11. Batist, P. A., Kapteijns, C. J., Lippens, B. C., and Schuit, G. C. A., *J. Catal.* **7**, 33 (1967).
12. Gai-Boyes, P. L., *Catal. Rev.–Sci. Eng.* **34**, 1 (1992).
13. Brückmann, K., Haber, J., and Wiltowski, T., *J. Catal.* **106**, 188 (1987).
14. Volta, J. C., and Tatibouet, J. M., *J. Catal.* **93**, 467 (1985).
15. Smith, M. R., and Ozkan, U. S., *J. Catal.* **141**, 124 (1993).
16. Guerrero-Ruiz, A., Blanco, J. M., Aguilar, M., Rodriguez-Ramos, I., and Fierro, J. L. G., *J. Catal.* **137**, 429 (1992).
17. Abon, M., Massardier, J., Mingot, B., Volta, J. C., Floquet, N., and Bertrand, O., *J. Catal.* **134**, 542 (1992).
18. Maciejewski, M., Baiker, A., and Reller, A., *Solid State Ionics* **43**, 203 (1990).
19. Firment, L. E., and Ferretti, A., *Surf. Sci.* **129**, 155 (1983).
20. Schlögl, R., *Angew. Chem. Int. Ed.* **32**, 381 (1993).
21. Ressler, T., Wienold, J., Jentoft, R. E., Neisius, T., and Günter, M. M., *Top. Catal.* **18**, 45 (2001).
22. Ressler, T., Timpe, O., Neisius, T., Find, J., Mestl, G., Dieterle, M., and Schlögl, R., *J. Catal.* **191**, 75 (2000).
23. Ressler, T., Wienold, J., and Jentoft, R. E., *Solid State Ionics* **141–142**, 243 (2001).
24. Ressler, T., Wienold, J., Jentoft, R. E., Timpe, O., and Neisius, T., *Solid State Commun.* **119**, 169 (2001).
25. Ressler, T., Jentoft, R. E., Wienold, J., Günter, M. M., and Timpe, O., *J. Phys. Chem. B* **104**, 6360 (2000).
26. Kraus, W., and Nolze, G., "PowderCell v2.3." Bundesanstalt für Materialforschung, Berlin, 0000.
27. Designed by M. Hagelstein, T. Neisius, *et al.*, ESRF, France, in a collaborative effort with the Fritz-Haber-Institut, Berlin, Germany, 1997.
28. Bearden, J. A., and Burr, A. F., *Rev. Mod. Phys.* **39**, 125 (1967).
29. Frahm, R., *Nucl. Instrum. Methods.* **A270**, 578 (1988).
30. Hagelstein, M., San Miguel, A., Fontaine, A., and Goulon, J., *J. Phys. IV* **7**, C2-303 (1997).
31. Hagelstein, M., Ferrero, C., Hatje, U., Ressler, T., and Metz, W., *J. Synch. Radiat.* **2**, 174 (1995).
32. Ressler, T., *J. Synch. Radiat.* **5**, 118 (1998).

33. Koningsberger, D. C., and Prins, R., "X-ray Absorption Spectroscopy, Chemical Analysis," Vol. 92. Wiley, New York, 1988.
34. Malinowski, E. R., and Howery, D. G., "Factor Analysis in Chemistry." Wiley, New York, 1980.
35. Ressler, T., Wong, J., Roos, J., and Smith, I. L., *Environ. Sci. Technol.* **34**, 950 (2000).
36. Rehr, J. J., Booth, C. H., Bridges, F., and Zabinsky, S. I., *Phys. Rev. B* **49**, 12347 (1994).
37. Ressler, T., Brock, S. L., Wong, J., and Suib, S. L., *J. Phys. Chem. B* **103**, 6407 (1999).
38. Blume, A., and Mestl, G., manuscript in preparation.
39. Vyazovkin, S., and Wight, C. A., *Annu. Rev. Phys. Chem.* **48**, 125 (1997).
40. Young, R. A., Ed., "The Rietveld Method," IUCr Monographs on Crystallography, Vol. 5. Oxford Univ. Press, Oxford, 1993.
41. Aso, I., Nakao, M., Yamazoe, N., and Seiyama, T., *J. Catal.* **57**, 287 (1979).
42. Smith, R. L., and Rohrer, G. S., *J. Catal.* **163**, 12 (1996).
43. Broclawik, E., and Haber, J., *J. Catal.* **72**, 379 (1981).
44. Tokarz-Sobieraj, R., Hermann, K., Witko, M., Blume, A., Mestl, G., and Schlögl, R., *Surf. Sci.* **489**, 107–125 (2001).
45. Cormack, A. N., Jones, R. M., Tasker, P. W., and Catlow, C. R. A., *J. Solid State Chem.* **44**, 174 (1982).
46. Kihlborg, L., *Ark. Kemi* **21**, 357 (1963).
47. Kihlborg, L., *Ark. Kemi* **21**, 443 (1963).
48. Kihlborg, L., *Ark. Kemi* **21**, 461 (1963).
49. Kihlborg, L., *Ark. Kemi* **21**, 365 (1963).
50. Bursill, L. A., *Proc. R. Soc. London Ser. A* **311**, 267 (1969).
51. Smith, R. L., and Rohrer, G. S., *J. Solid State Chem.* **124**, 104 (1996).
52. Gaigneaux, E. M., Ruiz, P., and Delmon, B., *Catal. Today* **32**, 37 (1996).
53. Sloczynski, J., *J. Solid State Chem.* **118**, 84 (1995).
54. Guerrero-Ruiz, A., Rodriguez-Ramos, I., Ferreira-Aparicio, P., Abon, M., and Volta, J. C., *Catal. Today* **32**, 223 (1996).
55. Floquet, N., Bertrand, O., and Heizmann, J. J., *Oxidation Met.* **37**, 253 (1992).
56. Haber, J., Marczewski, W., Stoch, J., and Ungier, L., *Ber. Bunsen-Ges. Phys. Chem.* **79**(11) 970 (1975).
57. Labanowska, M., *Phys. Chem. Chem. Phys.* **2**, 3307 (2000).
58. Mestl, G., Herzog, B., Schlögl, R., and Knözinger, H., *Langmuir* **11**, 3027 (1995).
59. Gai, P. L., Thoeni, W., and Hirsch, P. B., *J. Less-Common Met.* **54**, 263 (1979).
60. Bamford, C. H., ed., "Comprehensive Chemical Kinetics," Vol. 2. Elsevier, Amsterdam/New York, 1968.
61. Schmalzried, H., "Solid State Kinetics," VCH, Weinheim, 1994.
62. Jacobs, P. W. M., *J. Phys. Chem. B* **101**, 10086 (1997).
63. von Destinon-Forstmann, J., *Can. Metal. Q.* **4**, 1 (1965).
64. Haber, J., and Grzybowska, B., *J. Catal.* **28**, 489 (1973).
65. Sloczynski, J., and Bobinski, W., *J. Solid State Chem.* **92**, 436 (1991).
66. O'Keeffe, M., "Fast Ion Transport in Solids," p. 233. North-Holland, Amsterdam, 1973.
67. Volta, J. C., Bertrand, O., and Floquet, N., *J. Chem. Soc. Chem. Commun.* 1283 (1985).
68. Floquet, N., and Bertrand, O., *Surf. Sci.* **198**, 449 (1988).
69. Floquet, N., and Bertrand, O., *Solid State Ionics* **32/33**, 234 (1989).
70. Kahruman, C., Yusufoglu, I., and Oktay, E., *Trans. Inst. Min. Metall.* **108**, C8 (1999).
71. Ueno, A., and Bennett, C. O., *Bull. Chem. Soc. Jpn.* **52**, 2551 (1979).
72. Sancier, K. M., Wentrcek, P. R., and Wise, H., *J. Catal.* **39**, 141 (1975).